

ARTICLE OPEN



Gasdermin D-deficient mice are hypersensitive to acute kidney injury

Wulf Tonnus^{1,2}, Francesca Maremonti^{1,2}, Alexia Belavgeni^{1,2}, Markus Latk^{1,2}, Yoshihiro Kusunoki³, Anne Brucker^{1,2}, Anne von Mässenhausen^{1,2}, Claudia Meyer^{1,2}, Sophie Locke^{1,2}, Florian Gembardt¹, Kristina Beer^{1,2}, Paul Hoppenz^{1,2}, Jan U. Becker⁴, Christian Hugo¹, Hans-Joachim Anders³, Stefan R. Bornstein^{1,5,6,7,8}, Feng Shao⁹ and Andreas Linkermann^{1,2}✉

© The Author(s) 2022

Signaling pathways of regulated necrosis, such as necroptosis and ferroptosis, contribute to acute kidney injury (AKI), but the role of pyroptosis is unclear. Pyroptosis is mediated by the pore-forming protein gasdermin D (GSDMD). Here, we report a specific pattern of GSDMD-protein expression in the peritubular compartment of mice that underwent bilateral ischemia and reperfusion injury (IRI). Along similar lines, the GSDMD-protein expression in whole kidney lysates increased during the first 84 h following cisplatin-induced AKI. Importantly, unlike whole kidney lysates, no GSDMD-protein expression was detectable in isolated kidney tubules. In IRI and cisplatin-induced AKI, GSDMD-deficient mice exhibited hypersensitivity to injury as assessed by tubular damage, elevated markers of serum urea, and serum creatinine. This hypersensitivity was reversed by a combined deficiency of GSDMD and the necroptosis mediator mixed lineage kinase domain-like (MLKL). In conclusion, we demonstrate a non-cell autonomous role for GSDMD in protecting the tubular compartment from necroptosis-mediated damage in IRI.

Cell Death and Disease (2022)13:792; <https://doi.org/10.1038/s41419-022-05230-9>

INTRODUCTION

Acute kidney injury (AKI) emerges as a global health burden [1]. To allow the development of novel therapeutic strategies to treat AKI [2, 3] and prevent AKI-to-CKD (chronic kidney disease) transition [4], molecular insights into the mechanisms of failed tubular recovery, nephron loss and acute tubular necrosis (ATN) are required to allow future prevention medicine in those patients [3].

Regulated necrosis is mediated by a diverse set of cell death pathways [5]. In general, two separate systems have been delineated. Apoptosis, a caspase-regulated nonimmunogenic cell death that is not associated with the rupture of the plasma membrane [6], is tightly interconnected to two types of regulated necrotic cell death referred to as necroptosis [7, 8] and pyroptosis [9–14]. Necroptosis is mediated by kinases, such as RIPK1 [15, 16] and RIPK3 [17–19], and is executed by MLKL [20, 21] and counteracted by the ESCRT-III complex [22, 23]. Pyroptosis occurs downstream of inflammasome activation and is mediated by caspase-1/11-dependent cleavage of gasdermin D (GSDMD) [14, 24, 25]. N-terminal fragments of GSDMD were demonstrated to oligomerize and insert into the plasma membrane to mediate the loss of membrane integrity [25–28]. Importantly, pyroptosis, apoptosis, and necroptosis (jointly also

referred to as PANoptosis [29]) exhibit a complex system of host defense against viruses [30] and bacteria [31].

In contrast to the signaling system of pyroptosis, apoptosis, and necroptosis, a separate system exists referred to as ferroptosis, death by lipid peroxidation following iron-catalyzed Fenton reactions [32, 33]. In contrast to other pathways, cell death during ferroptosis was demonstrated to follow intercellular osmotic patterns of cell death propagation [34–37], thereby affecting functional units, such as the synchronized death of renal tubules [38], rather than individual cells.

In acute kidney injury models, such as cisplatin-induced AKI and ischemia-reperfusion injury, the roles of ferroptosis, apoptosis, and necroptosis have been subject to extensive investigations over the last decades [39–41]. However, the role of pyroptosis in AKI was hardly explored, and the limited existing results are controversial [42–46].

Here, we demonstrate a unique peritubular pattern of GSDMD expression during AKI and show GSDMD-deficient mice to be hypersensitive to IRI and cisplatin-induced AKI. Mechanistically we identify this hypersensitization to be mediated by MLKL-dependent necroptosis.

¹Department of Internal Medicine 3, University Hospital Carl Gustav Carus at the Technische Universität Dresden, Dresden, Germany. ²Biotechnology Center, Technische Universität Dresden, Dresden, Germany. ³Renal Division, Department of Medicine IV, University Hospital of the Ludwig Maximilian University, Munich, Germany. ⁴Institute of Pathology, University Hospital of Cologne, Cologne, Germany. ⁵Diabetes and Nutritional Sciences, King's College London, London, UK. ⁶Center for Regenerative Therapies, Technische Universität Dresden, Dresden, Germany. ⁷Paul Langerhans Institute Dresden of Helmholtz Centre Munich at University Clinic Carl Gustav Carus of TU Dresden Faculty of Medicine, Dresden, Germany. ⁸Lee Kong Chian School of Medicine, Nanyang Technological University, Singapore, Singapore. ⁹National Institute of Biological Sciences (NIBS), Beijing, China. ✉email: andreas.linkermann@ukdd.de

Edited by Professor Mauro Piacentini

Received: 3 July 2022 Revised: 30 August 2022 Accepted: 2 September 2022

Published online: 15 September 2022

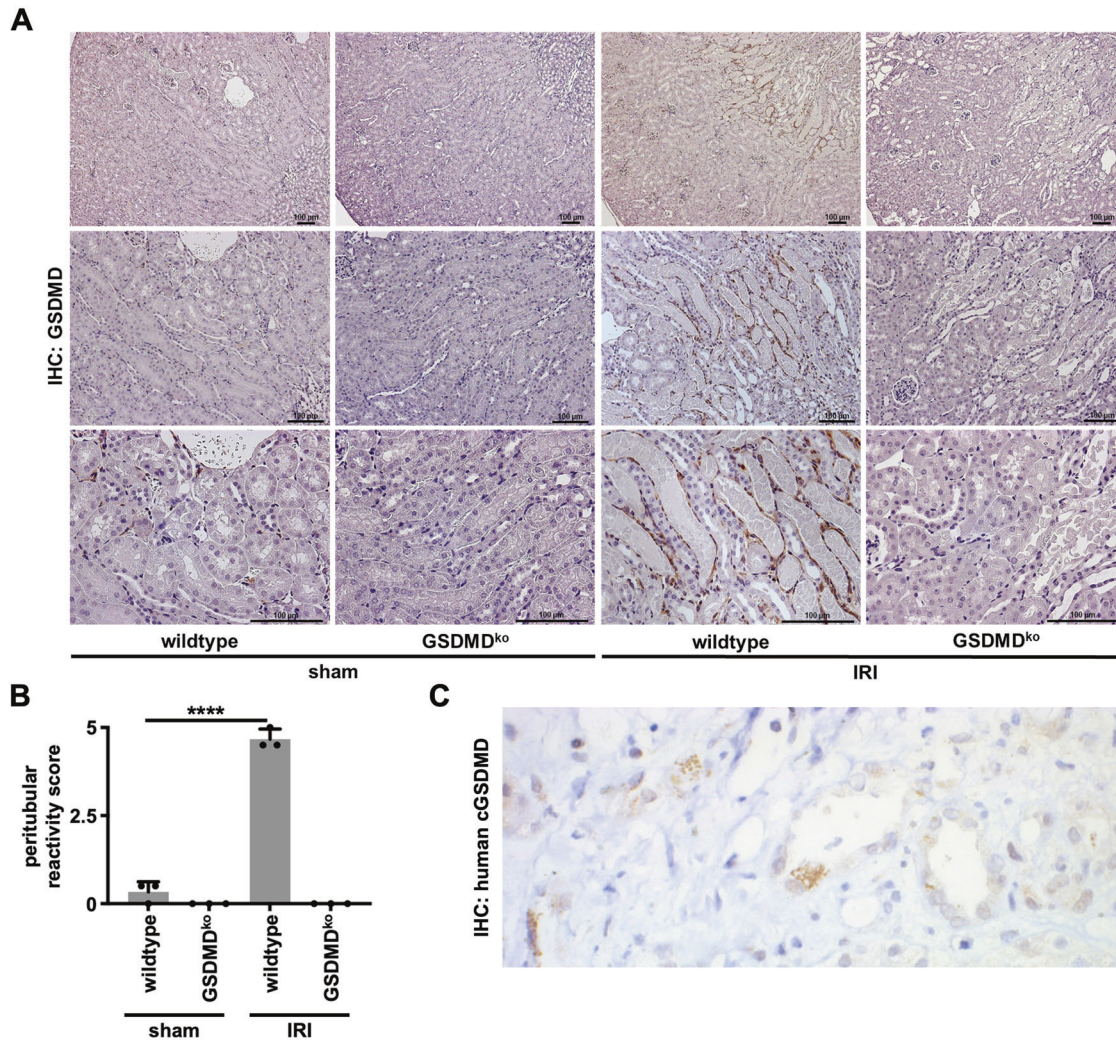


Fig. 1 Gasdermin D-positivity in murine and human renal AKI. Eight- to twelve-week-old male wild-type and *Gsdmd*-deficient mice underwent severe IRI and were evaluated after 48 h. **A** Immunohistochemistry (IHC) for GSDMD reveals specific peritubular positivity lining necrotic tubules. **B** Quantification of peritubular GSDMD reactivity. ($n = 3$ mice/group) (Student's t -test for **** $p < 0.0001$). **C** Human biopsy IHC for cleaved gasdermin D in an AKI patient sample.

RESULTS

Ischemia-reperfusion injury induces gasdermin D (GSDMD) expression in the peritubular compartment of necrotic segments

GSDMD was identified as the major downstream mediator of pyroptosis. We, therefore, stained sections obtained from male C57Bl/6N mice that underwent bilateral renal ischemia-reperfusion injury (IRI) for GSDMD by immunohistochemistry. In order to detect potential off-target staining of the antibody, *Gsdmd*-deficient mice served as controls (Fig. 1A and Fig. S1). While the baseline expression of GSDMD appeared minimal, we observed a strictly peritubular staining pattern of GSDMD within 48 h following the onset of reperfusion. This pattern appeared particularly dominant next to areas of extensive acute tubular necrosis in the S3 segment of the proximal tubule, while no signal at all was detected in the sections obtained from *Gsdmd*-ko mice (Fig. 1B). Additionally, the cleaved N-terminal fragment of GSDMD was detectable in indication biopsies of patients suffering from AKI (Fig. 1C).

To investigate the pyroptotic proteins in AKI, we generated *Gsdmd*- and gasdermin E (*Gsdme*)-deficient mice and crossed them to obtain *Gsdmd*/*Gsdme* double-deficient littermates. Among untreated animals of these genotypes, the investigation of renal tissue by periodic acid-Schiff (PAS) staining revealed no obvious

histological signs of tubular damage or any detectable phenotype (Fig. S2A). In line with this observation, the concentrations of both serum creatinine (Fig. S2B) and serum urea (Fig. S2C) were indistinguishable from wild-type littermates.

Genetic deficiency of GSDMD, GSDME, or combined deficiency hypersensitizes mice to IRI-induced AKI

We investigated *Gsdmd*-, *Gsdme*-, and double-deficient mice in a standard model of moderate bilateral IRI (compare methods section for details). In comparison to wild-type mice, significantly aggravated necrotic regions in the S3 segment of the proximal tubules and the outer stripe of the inner medulla, as detected by PAS staining, were observed (Fig. 2A, B). In keeping with this observation, we discovered a significantly larger increase in serum concentrations of creatinine (Fig. 2C) and urea (Fig. 2D) in *Gsdmd*- and *Gsdme*-deficient mice compared to wild-types. Similar values were detected upon combined deficiency of GSDMD and GSDME. Clinically, the ischemic dose that leads to nephron loss may vary considerably between individuals. We, therefore, added a set of separate experiments with an increased dose of ischemia before reperfusion, referred to as severe IRI. However, no significant differences between wild-type and *Gsdmd*-deficient mice were detectable after 24 h or 48 h by PAS staining (Fig. S3A, B) or functional markers of renal injury (Fig. S3C, D).

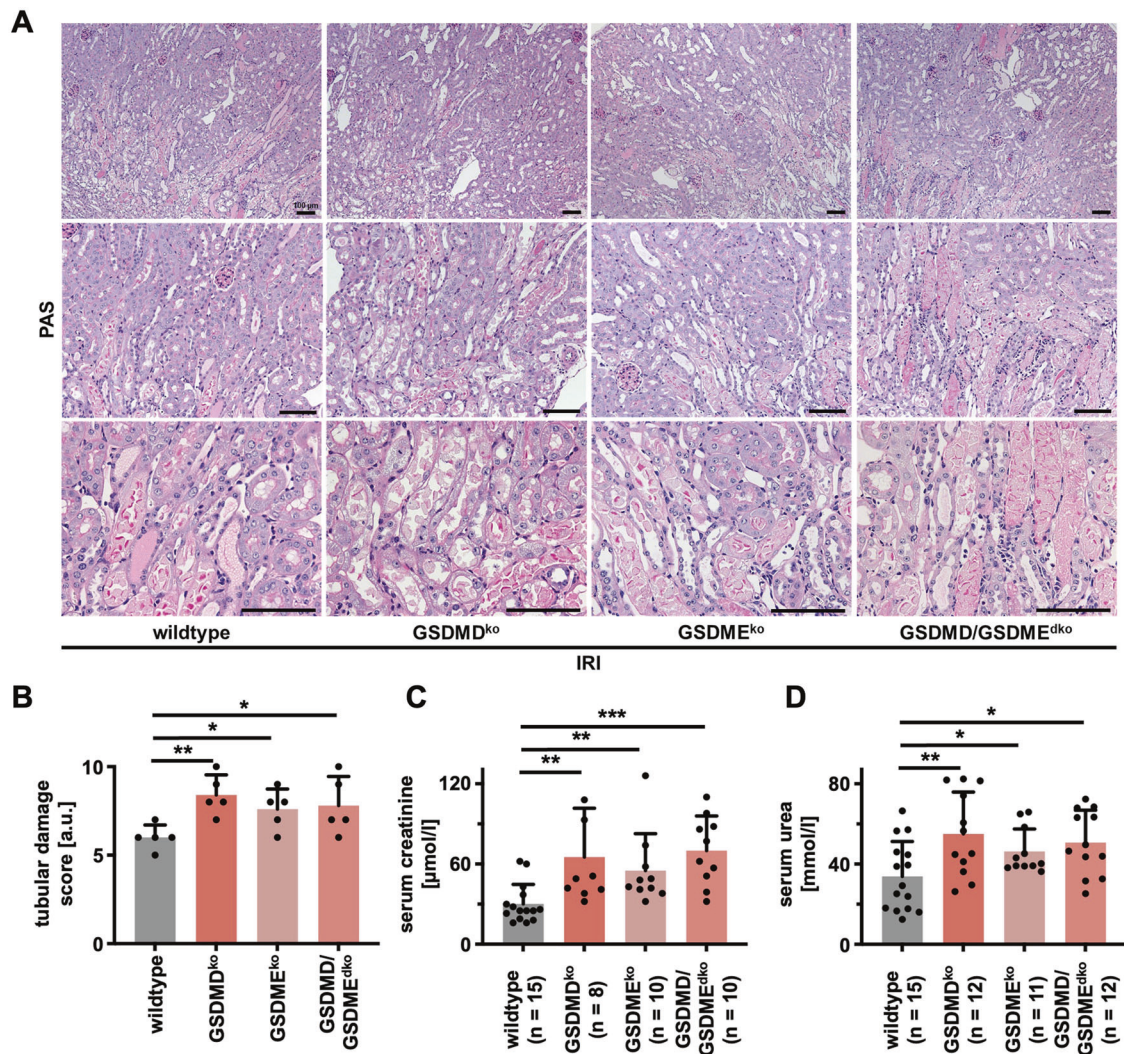


Fig. 2 Deficiency of gasdermin D, gasdermin E, or the combined deficiency sensitizes to ischemia-reperfusion-induced acute kidney injury. Eight- to twelve-week-old male wild-type, *Gsdmd*^{ko}, *Gsdme*^{ko}, and *Gsdmd/Gsdme*^{diko} mice underwent moderate IRI and were sacrificed after 48 h of reperfusion. **A** Histological evaluation revealed increased tubular damage in comparison to wild-type mice, quantified by tubular damage scores (**B**). Serum creatinine (**C**) and serum urea (**D**) concentrations upon sacrifice 48 h after the onset of reperfusion. Note the reduced kidney function in *Gsdmd*^{ko}, *Gsdme*^{ko}, and *Gsdmd/Gsdme*^{diko} mice. (n = 8–15 mice/group) (Student's t-test for **p* < 0.05, ***p* < 0.01, ****p* < 0.001).

In addition, we detected no significant difference in post-IRI numbers of infiltrating CD3 cells (Fig. S4A, B) upon assessment of severe IRI. In summary, these results suggest that the genetic deficiency of GSDMD correlates with the loss of a protective non-cell autonomous signal that aggravates the outcome following IRI in mice.

As demonstrated above, immunohistochemistry demonstrated no tubular expression of GSDMD (Fig. 1A). Therefore, we hypothesized that the tubular injury may develop secondarily and independently of GSDMD. To test this hypothesis, we isolated renal tubules from *Gsdmd*⁻, *Gsdme*⁻, and double-deficient littermates and investigated morphological changes over 6 h. As demonstrated in Fig. 3A, no major morphological differences were observed between these groups. Along similar lines, the LDH released from these tubules exhibited no significant differences between the groups (Fig. 3B). Importantly, and in line with the previous observation, we failed to detect GSDMD by western blotting from lysates of kidney tubules, while a clear band at the expected size appeared in control HT1080 cells and whole kidney lysates (Fig. 3C). These results suggest a lack of GSDMD expression in the tubular compartment.

Hypersensitization to IRI in *Gsdmd*-deficient mice is reversed by combined genetic deletion of the necroptosis-executor mixed lineage kinase domain-like (MLKL)

It has been demonstrated by us and others that pyroptosis and necroptosis are interconnected and cross-regulated signaling pathways of regulated necrosis [31, 47–49]. We, therefore, speculated that *Gsdmd*-deficiency might activate the necroptosis pathway, which we previously demonstrated to be involved in AKI at the level of RIPK1 [50], RIPK3 [51], MLKL [52], and ESCRT-III [22]. Thus, we crossed *Gsdmd*-deficient mice with MLKL-deficient mice in our facility and observed no spontaneous histological and functional differences between wild-type, *Gsdmd*-ko and *Mkl1/Gsdmd*-dco kidneys (Fig. S5A–C). In line with our hypothesis, the co-deficiency of MLKL in addition to GSDMD reversed the increased tubular morphological changes observed in GSDMD-ko mice challenged with IRI (Fig. 4A, B). Furthermore, serum concentrations of creatinine (Fig. 4C) and urea (Fig. 4D) in *Mkl1/Gsdmd*-dco mice were kept at the level of wild-type mice in this model. These data suggest an in vivo interplay between pyroptosis and necroptosis.

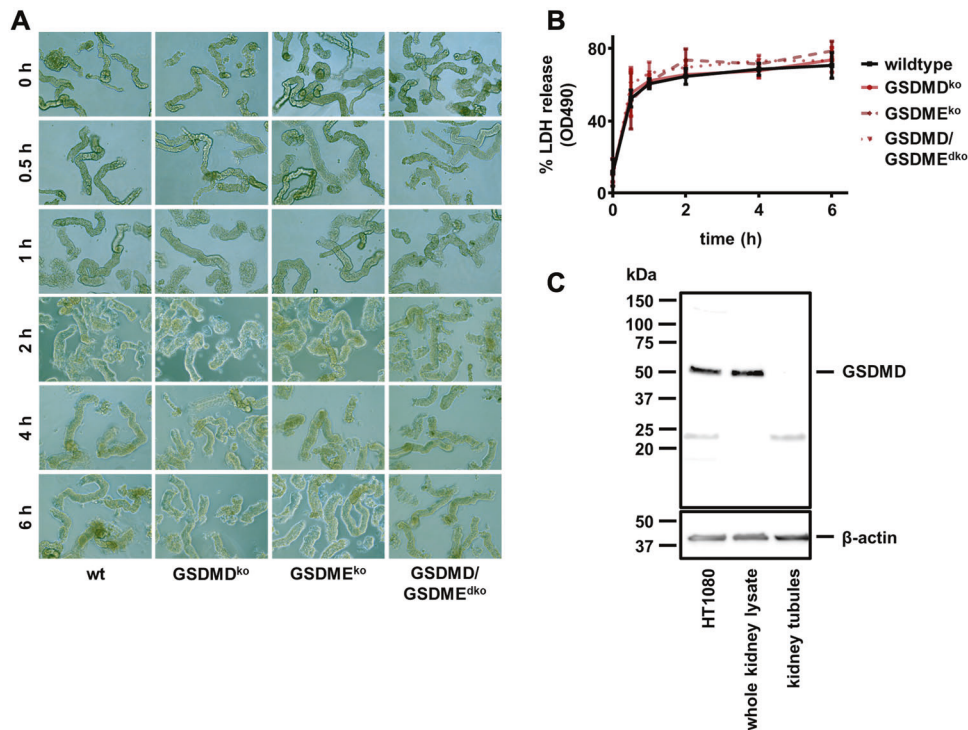


Fig. 3 Gasdermin D is not detectable in murine kidney tubules and is not involved in tubular necrosis. **A** Still images of freshly isolated tubules from male wild-type, *Gsdmd*^{ko}, *Gsdme*^{ko}, and *Gsdmd/Gsdme*^dko mice at indicated time points (0 h until 6 h) after preparation. **B** LDH release into the medium was quantified over time without significant differences. **C** Western blot of murine GSDMD. Note the absence of the GSDMD band in lysates from freshly isolated renal tubules. ($n = 2$ independent experiments/group).

A GSDMD-to-MLKL switch mechanism hypersensitizes *Gsdmd*-deficient mice to cisplatin-induced renal injury

To investigate the role of GSDMD in a distinct AKI model, we subjected wild-type mice to intraperitoneal injection of 20 mg/kg body weight cisplatin (cisplatin-induced AKI) and separated the mice into eight distinct groups. Mice were sacrificed after 0, 12, 24, 36, 48, 60, 72 and 84 h. Serum levels of creatinine (Fig. 5A) and urea (Fig. 5B) were obtained at these time points, and whole kidney lysates were generated following euthanasia. We previously demonstrated the time course of p38 and phospho-p38 MAP kinase activation in renal tissue following IRI [38]. As demonstrated in Fig. 5C, D, we observed a comparable pattern of the induction of GSDMD-protein expression within 84 h.

We next compared wild-type mice alongside *Gsdmd*-ko and *Mkl1/Gsdmd*-dco mice in the model of cisplatin-induced AKI. As observed in the model of IRI, *Gsdmd*-ko were hypersensitive to tubular damage 48 h after injection (Fig. 6A, B), and functional markers of AKI were significantly increased (Fig. 6C, D). Again, genetic co-deletion of MLKL reversed these features to the level of wild-type mice (Fig. 6A, D). Finally, we compared the overall survival of wild-type, *Gsdmd*-ko, and *Mkl1/Gsdmd*-dco following cisplatin injection (Fig. 6E). While *Gsdmd*-ko mice succumbed significantly earlier than wild-type mice, the survival of *Mkl1/Gsdmd*-dco mice was comparable to wild-type mice.

The mouse model of cisplatin-mediated AKI was repeatedly demonstrated to depend on a TNF α -signal, and interference with TNF (e.g., by etanercept) is known to partially protect mice in this model [53–55]. In addition, *Gsdmd*-deficient mice are resistant to the TNF α -induced SIRS model [10]. To re-evaluate published data on cisplatin-induced AKI, we reduced the cisplatin dose to 15 mg/kg body weight. While in wild-type littermates, the effect of etanercept was solidly reproducible, and *Gsdme*-deficient mice exhibited no significant difference in this model (Fig. S6A), we detected no significant difference through the addition of etanercept in *Gsdmd*-deficient mice (Fig. S6B). Together with

previously published data on the role of GSDMD in the TNF α -induced SIRS model [10], our data indicate that, again, distinct TNF α -dependent effects rely on GSDMD.

Gsdmd-deficient mice are hypersensitive to calcium oxalate-induced chronic nephropathy

To test a third model of subacute AKI that transfers into chronic kidney disease (CKD), we investigated the effects of *Gsdmd*-deficient mice in a mouse model of AKI induced by calcium oxalate (CaOx). The glomerular filtration rate (GFR) measured at 20 days following the onset of a CaOx-enriched diet (see methods section for details) showed a significant decrease only in the *Gsdmd*-deficient mice (Fig. S7A). In keeping with this observation, the functional kidney markers of serum creatinine and urea (BUN) were increased (Fig. S7B, C), although this effect did not reach statistical significance. Importantly, the mRNA levels of the kidney tubular damage marker NGAL were indistinguishable (Fig. S7D). Collectively, these data indicate that genetic deficiency of the pyroptosis executor protein GSDMD sensitizes to acute kidney injury in three independent rodent models.

DISCUSSION

Acute kidney injury is known to be partially mediated by necroptosis and ferroptosis, two signaling pathways of regulated necrosis [39]. The NLRP3 inflammasome [56, 57] and GSDMD-mediated pyroptosis [47] were demonstrated to comprise common regulatory motifs with necroptosis [58]. In this sense, GSDMD is regulated and can be cleaved by caspase-8 [10, 59–62]. Hence, we did not directly address the question of which protease processes GSDMD in our specific models. Also, in response to virally infected cells, necroptosis and pyroptosis regulate an intertwined system [63, 64]. It has recently been demonstrated that macrophages carrying a *Lrrk2*G2019S mutation display plasticity between pyroptosis and necroptosis, which is mediated by translocation of cGSDMD to mitochondria to form ROS-releasing pores [65]. The release of mitochondrial ROS was

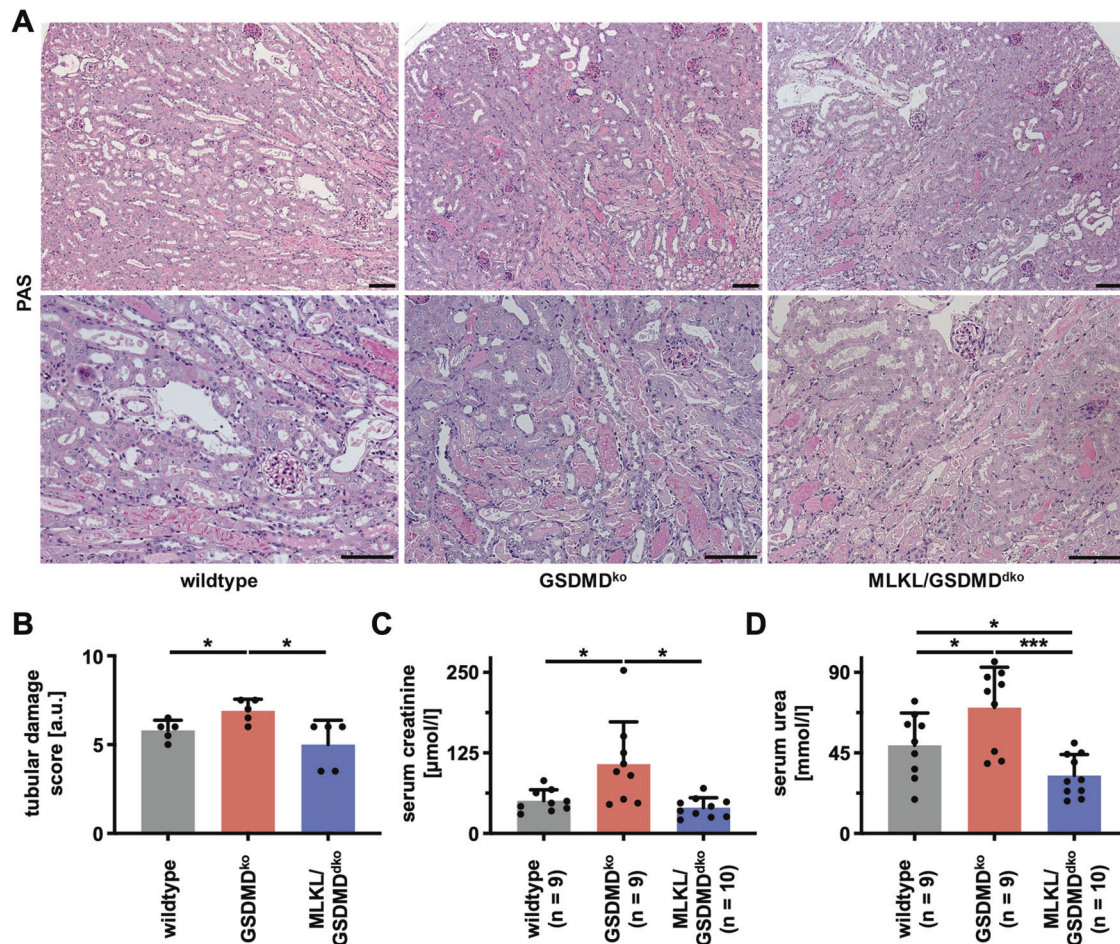


Fig. 4 Co-deletion of the necroptosis-executor MLKL reverses hypersensitivity toward IRI of *Gsdmd*-deficient mice. Male 8–12-week-old wild-type, *Gsdmd*^{ko}, and *Mlkl/Gsdmd*^{diko} mice underwent moderate IRI. **A, B** At 48 h after the onset of reperfusion, histology demonstrated reduced tubular damage in *Mlkl/Gsdmd*^{diko} mice as quantified by tubular damage score. **C, D** Co-deletion of MLKL also significantly decreased serum concentrations of creatinine and urea. ($n = 9$ – 10 mice/group) (Student's *t*-test for * $p < 0.05$; ** $p < 0.01$; *** $p < 0.001$).

postulated to promote necroptosis by increased phosphorylation of RIPK3. However, it remains unclear whether such plasticity exists in wild-type macrophages and how mitochondrial ROS might lead to the phosphorylation of RIPK3. To the best of our knowledge, crosstalk between necroptosis and pyroptosis has not been investigated in AKI. In fact, we previously investigated an interference with mitochondrial permeability transition (*ppif*-deficiency) alongside the induction of necroptosis and reported that these are distinct pathways that are activated in parallel during AKI [51]. Recently, we demonstrated ROS scavenging by lipophilic radical trapping agents to increase rather than reduce the phosphorylation of RIPK1 and MLKL upon necroptosis induction in HT29 cells [66]. Therefore, our data do not support a “pyroptosis-to-necroptosis switch” within a single cell, such as a macrophage, to be of significant relevance to AKI models. Here, however, we demonstrate the first evidence of pyroptosis and necroptosis to function in different cell types during AKI to prevent further deterioration and propagation of tubular damage. Rather than being primarily involved in renal tubular epithelial cell death, GSDMD-positive cells may constrain necroptotic cell death in the tubules. However, the exact mechanism of these functions remains to be elucidated in future studies.

Recently, the FDA-approved drug disulfiram was demonstrated to inhibit pyroptosis by interfering with the pore-forming activity of cleaved GSDMD [67]. Although, to the best of our current knowledge, disulfiram has not been investigated in AKI models, it has been demonstrated to augment oxidative stress in rat brains following bilateral carotid artery occlusion [68]. Our data that point to a non-cell

autonomous tissue-protective function of GSDMD are in line with those discoveries. However, two recent publications suggested that the genetic deficiency of GSDMD or the inhibition of the NLRP3 inflammasome may be protective in models of AKI and protect from tubular necrosis [42, 43]. Our data are in contrast to those publications and in line with post-IRI single-cell analysis that failed to detect GSDMD expression in tubular epithelial cells following murine kidney IRI [69]. Interestingly, another paper demonstrated an increase of the N-terminal fragment of GSDMD over the time course of 48 h after IRI [70], which is in line with our results from both IRI and cisplatin-induced AKI. A possible explanation for the different conclusions may be the lower number of mice per group [42, 43, 70] and the differences in severities of the AKI models [42, 43, 70]. In this regard, we consider it particularly important to reconcile the absence of GSDMD expression in renal tubules (Fig. 1A and Fig. 3C).

In conclusion, we demonstrated GSDMD to be upregulated in the peritubular compartment, specifically next to necrotic tubular epithelial cells, to function as a suppressor of AKI by a previously unknown non-cell autonomous crosstalk to the necroptosis machinery. These data add yet another layer of complexity to the pathogenesis of AKI.

MATERIALS AND METHODS

Cells and reagents

The human HT1080 cell line was purchased from the American Type Culture Collection. Cells were cultured in a humidified 5% CO₂ atmosphere

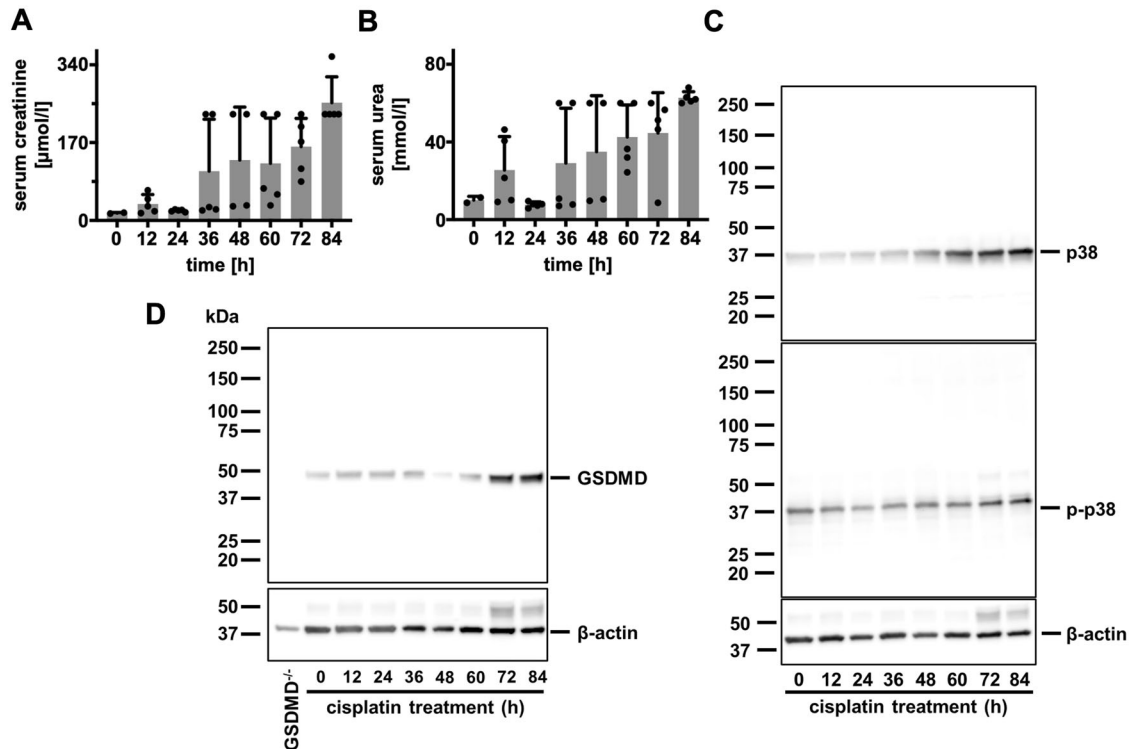


Fig. 5 Gasdermin D-positivity increases over time in cisplatin-induced AKI. Eight- to twelve-week-old female wild-type mice ($n = 5$ mice/ time point) were treated with 20 mg/kg body weight cisplatin intraperitoneally. **A, B** At indicated time points, mice were sacrificed and serum concentrations of creatinine and urea were measured. **C** Corresponding western blot analysis of whole kidney lysates stained for p38 MAP kinase and phospho-p38 MAP kinase (p-p38). **D** Corresponding Western Blot analysis of whole kidney lysates demonstrates increased GSDMD expression over time.

and cultured in Dulbecco's modified Eagle medium (DMEM, Thermo Fisher) supplemented with 10% (v/v) FBS (Thermo Fisher), 100 U/ml penicillin, and 100 μg/ml streptomycin (Pen/Strep, Thermo Fisher).

Western blotting

Cells were lysed in ice-cold 10 mM Tris-HCl, pH 7.5, 50 mM NaCl, 1% Triton X-100, 30 mM sodium pyrophosphate, 50 mM NaF, 100 μM Na_3VO_4 , 2 μM ZnCl_2 , and 1 mM phenylmethylsulfonyl fluoride (PMSF, modified Frackelton buffer) for 30 min on ice. Insoluble material was removed by centrifugation (14,000 × g , 30 min, 4 °C). Protein concentration was determined using a commercial Bradford assay kit according to the manufacturer's instructions (Thermo Fisher). Equal amounts of protein were resolved on a 4–15% gradient SDS/PAGE gel and transferred to a PVDF membrane (BIO-RAD). Mouse kidneys were cut in half immediately after the sacrifice of the mice and placed in tubes containing beads and ice-cold modified Frackelton buffer. The tubes were transferred to a bead mill homogenizer, and samples were homogenized. Equal amounts of protein (typically 35 μg per lane) were incubated with Roti-Load 1 (ROTH), resolved on a 4–15% gradient SDS/PAGE gel, and transferred to a PVDF membrane (BIO-RAD). Isolated primary murine tubules (see Isolation of primary murine renal tubules section) were incubated with Roti-Load 1 (ROTH) and resolved on a 4–15% gradient SDS/PAGE gel and transferred to a PVDF membrane (BIO-RAD). Primary antibody incubation was performed for GSDMD (Abcam, ab219800), p38 MAPK (Cell Signaling, Cat# 9212), phospho-p38 MAPK (Cell Signaling, Cat# 4511), and anti-β-Actin (Cell Signaling, Cat# 3700 S) at concentrations 1:1000. Secondary antibodies (anti-mouse, HRP-linked antibody, Cell Signaling, Cat# 7076 S; anti-rabbit, HRP-linked antibody, Cell Signaling, Cat# 7074 S) were applied at concentrations of 1:5000. Proteins were then visualized by enhanced chemiluminescence (ECL; Amersham Biosciences). All data presented in the manuscript are representative examples of at least three biological replicates of the specific experiment.

Mice

All mice referred to as wild-types (WT) in this study are C57Bl/6N obtained from Charles River Laboratories (Sulzfeld, Germany). *Gsdmd*-deficient mice [24] and *Gsdme*-deficient mice [71] were described earlier

and crossed to generate *GSDMD/GSDME*^{dko} mice. *GSDMD*^{ko} mice were additionally crossed to *Mikl*^{ko} mice, kindly provided by James Murphy [72], to generate *Mikl/Gsdmd*^{dko} mice. To minimize background effects, *Mikl/Gsdmd*^{dko} mice were interbred for at least 10 generations before including them in experiments. All in vivo experiments were performed according to the Protection of Animals Act, after approval of the German local authorities in Dresden and Munich (TVV57/2017). Group sizes were calculated beforehand with the help of a professional statistician from the Institute of Medical Informatics and Biometry of the Technische Universität Dresden. In all experiments, mice were rigorously matched for age, sex, weight, and genetic background and used as indicated in each individual experiment. Thus, all genetically modified mice used in experiments were genotyped by PCR, and investigators were strictly unaware of the genotype and experimental groups until data collection was completed.

Murine ischemia/reperfusion injury (IRI)

The technique has been previously described in detail [73]. Concisely, 8–12-week-old male mice were co-housed at 2–5 mice/ cage in IVCs in our facility under 12 h light circles. Induction of kidney IRI was performed via a midline abdominal incision and a bilateral renal pedicle clamping for either 36 min (severe IRI) or 30 min (moderate IRI) using microaneurysm clamps (FST). Throughout the surgical procedure, the body temperature was maintained between 36 °C and 37 °C by continuous monitoring using a temperature-controlled self-regulated heating system (Fine Science Tools). After the removal of the clamps, reperfusion of the kidneys was confirmed visually. The abdomen was closed in two layers using standard 6-0 sutures. Sham-operated mice underwent identical surgical procedures, except that microaneurysm clamps were not applied. To maintain fluid balance, all mice were supplemented with 1 mL of prewarmed PBS administered intraperitoneally directly after surgery. Mice were put back in cages in pairs of 2 and monitored closely. After 48 h, retro-orbital blood collection was performed, and mice were sacrificed by cervical dislocation. The right kidney was put in 4% formaldehyde for 24 h and then transferred to 70% ethanol for storage. Correspondingly, the left kidney was snap-frozen.

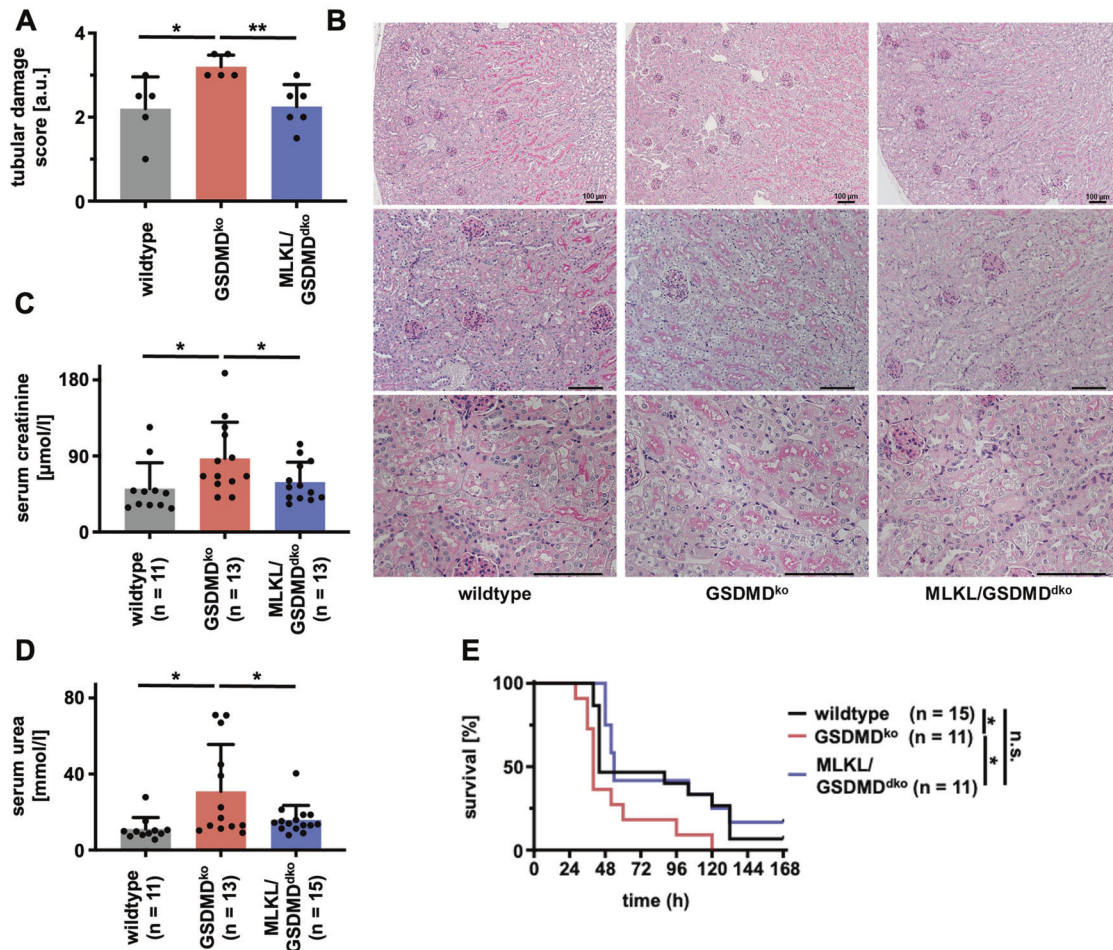


Fig. 6 Co-deletion of MLKL reverses the hypersensitivity of *Gsdmd*-deficient mice in cisplatin-induced AKI. Female 8–12-week-old wild-type, *Gsdmd*^{ko}, and *Mkl/Gsdmd*^{dko} mice were treated with 20 mg/kg body weight of cisplatin i.p. **A, B** After 48 h, mice were sacrificed, histological sections were stained for PAS, and tubular damage was quantified. Note the deterioration of tubular damage in *Gsdmd*^{ko}-mice compare to wild-type mice, which was reversed in *Mkl/Gsdmd*^{dko} mice. **C, D** Serum concentrations of creatinine and urea at 48 h after the onset of reperfusion in indicated groups. **E** Kaplan–Meier survival plot of indicated groups of mice following a single injection of cisplatin. Note the significant survival benefit between the *Gsdmd*^{ko}-mice and *Mkl/Gsdmd*^{dko}-mice. The latter are no different from wild-type mice. ($n = 11$ –15 mice/group) (Student's *t*-test or log-rank test with * $p < 0.05$, ** $p < 0.01$).

Murine cisplatin-induced acute kidney injury

Eight- to twelve-week-old female mice were co-house at 2–5 mice/ cage in IVCs in our facility under 12 h light circles. As reported earlier [73], females were rigorously matched for weight, age, and genetic background to receive single dose cisplatin (20 mg/kg body weight if not otherwise indicated) intraperitoneally in a volume of 400 µl. After injection, mice were put back in cages at 2–5 animals and monitored closely. After 48 h, retro-orbital blood collection was performed, and mice were sacrificed by cervical dislocation. The right kidney was put in 4% formaldehyde for 24 h and then transferred to 70% ethanol for storage. Correspondingly, the left kidney was snap-frozen. For survival analysis, mice were closely monitored for up to 7 days. If prespecified parameters of severe animal deterioration were met, mice were considered dead and were sacrificed according to German animal protection laws.

Histology and evaluation of structural organ damage

For histology, the kidneys were dehydrated in a graded ethanol series and xylene and finally embedded in paraffin. Paraffin sections (3–5 µm) were stained with periodic acid-Schiff (PAS) reagent, according to standard routine protocol. Stained sections were analyzed using an Axio Imager microscope (Zeiss) at $\times 100$, $\times 200$, and $\times 400$ magnification. Micrographs were digitalized using an AxioCam MRm Rev. 3 FireWire camera and AxioVision ver. 4.5 software (Zeiss). Organ damage was quantified by two experienced pathologists in a double-blind manner on a scale ranging from 0 (unaffected tissue) to 10 (severe organ damage).

For the scoring system, tissues were stained with PAS, and the degree of morphological involvement in renal failure was determined using light microscopy. The following parameters were chosen as indicative of morphological damage to the kidney after ischemia-reperfusion injury (IRI): brush border loss, tubule dilatation, tubule degeneration, tubule necrosis, and tubular cast formation. These parameters were evaluated on a scale of 0–10, which ranged from not present (0), mild (1–4), moderate (5 or 6), severe (7 or 8), to very severe (9 or 10). The following parameters were chosen as indicative of morphological damage to the kidney after cisplatin injection: brush border loss, red blood cell extravasation, tubule dilatation, tubule degeneration, tubule necrosis, and tubular cast formation. These parameters were evaluated on a scale of 0–4, which ranged from not present (0), mild (1), moderate (2), severe (3), to very severe (4). Each parameter was determined on at least five different animals per group.

Immunohistochemistry (IHC)

Organs (mouse or human) were dissected and transferred into 4% (vol/vol) neutral buffered formaldehyde, fixed for 24 h, and subsequently transferred to 70% ethanol. For histology, the kidneys were dehydrated in a graded ethanol series and xylene and finally embedded in paraffin. The sections (1.5 µm) were then deparaffinized, rehydrated, and boiled in citrate buffer pH 6 for 5 min (DC module 110 °C, Biocare). After 30 min cooling in a water bath, the slides were washed and treated with 3% H₂O₂ followed by blocking in 1% BSA for 1 h. Sections were then incubated o/n with anti-GSDMD (Abcam, ab219800) antibody (1:500 in 1% BSA) or anti CD3 (Dianova, DIA-P3E) antibody (1:200 in 1% BSA without antigen retrieval).

The primary antibody was detected using a secondary goat anti-rabbit antibody (Abcam, ab214880; 1 h at room temperature) and the DAB substrate kit (Abcam ab64238; 5 min). After counterstaining with hematoxylin (1 min), sections were analyzed using an Axio Imager microscope (Zeiss) and AxioVision version 4.5 software (Zeiss). For negative controls, the primary antibody was omitted and replaced with a blocking solution.

Mouse model of calcium oxalate-induced acute kidney injury

Male 8-week-old *Gsdmd*-deficient mice and WT mice received an oxalate-rich diet for 20 days. Oxalate-rich diet was prepared by adding 50 $\mu\text{mol/g}$ sodium oxalate to a calcium-free standard diet (Ssniff, Soest, Germany). Mice were sacrificed by cervical dislocation on day 20 after initiation of the CaOx-enriched diet as described [74]. Plasma samples were collected, and GFR was measured at baseline and before sacrifice. Kidneys were harvested after sacrifice and kept in RNA later solution at -20°C .

GFR measurements were performed in conscious mice on days 0 and 20 as described [75]. Therefore, mice were anesthetized with isoflurane to mount a miniaturized imager device built from two light-emitting diodes, a photodiode and a battery (MediBeacon, Mannheim, Germany), onto the shaved neck of the animals. The background signal of the skin was recorded for 5 min. Subsequently, mice received an intravenous injection of 150 mg/kg FITC-sinistrin (MediBeacon, Mannheim, Germany). During the entire process, mice were conscious and kept in a single cage, and the signal was recorded for 90 min. Data were analyzed using MPD Lab software (MediBeacon, Mannheim, Germany). The GFR [$\mu\text{l}/\text{min}$] was calculated from the decrease of fluorescence intensity over time using a two-compartment model, the animals' body weight, and an empirical conversion factor [76].

Real-time PCR

To assess mRNA expression levels, total RNA was isolated from kidneys using an RNA extraction kit (Invitrogen, USA) following the manufacturer's instructions. RNA quality was assessed using agarose gels before transcription into cDNA using reverse transcriptase (Superscript II; Invitrogen, Carlsbad, CA, USA). Real-time quantitative PCR was performed using SYBRGreen PCR master mix, analyzed with Light Cycler 480 (Roche, Mannheim, Germany). Gene expression values were normalized using 18 s rRNA as a housekeeping gene. The primers used for amplification were purchased from Metabion (Martinsried, Germany) and are listed below.

Target	Primer sequences
18 s	Forward: 5'-GCAATTATTCCTCATGAA-3'
	Reverse: 5'-AGGGCCTCACTAAACCAT-3'
NGAL	Forward: 5'-ATGTCACCTCCATCCTGG-3'
	Reverse: 5'-GCCACTGCACATTGTAG-3'

Isolation of fresh murine tubules

Primary murine renal tubules were isolated following a modified previously published protocol [38]. Briefly, murine kidneys were removed, washed with PBS, decapsulated, and sliced in four to five slices. Kidney slices of each kidney were transferred in 2 ml tubes containing 2 mg/ml collagenase type II in incubation solution (48 $\mu\text{g}/\text{ml}$ trypsin inhibitor, 25 $\mu\text{g}/\text{ml}$ DNase I, 140 mM NaCl, 0.4 mM KH_2PO_4 , 1.6 mM $\text{K}_2\text{HPO}_4 \times 3 \text{H}_2\text{O}$, 1 mM $\text{MgSO}_4 \times 7 \text{H}_2\text{O}$, 10 mM $\text{CH}_3\text{COONa} \times 3 \text{H}_2\text{O}$, 1 mM α -ketoglutarate and 1.3 mM Ca-gluconate) and digested for 5 min at 37°C , 850 rpm. In order to minimize the presence of damaged tubules, the first resulting supernatant was discarded. Afterward, 1 ml of 2 mg/ml collagenase type II in incubation solution was added to the kidney slices and digested for 5 min at 37°C , 850 rpm. The supernatant was collected and transferred in a 2 ml tube containing 1 ml ice-cold sorting solution (0.5 mg/ml bovine albumin in incubation solution). Tubes were left on ice for the tubules to precipitate. The supernatant was removed, and the tubules were washed twice with an ice-cold incubation solution. After precipitation of the tubules, the supernatant was removed, and an ice-cold sorting solution was added (volume was adjusted depending on the number of samples needed for the experiment). Tubules were distributed in a 24-well plate containing Dulbecco's Modified Eagle Medium F-12 Nutrient Mixture without glycine and phenol red (DMEM/F-12, Thermo Fischer),

supplemented with 0.01 mg/ml recombinant human insulin, 5.5 $\mu\text{g}/\text{ml}$ human transferrin, 0.005 $\mu\text{g}/\text{ml}$ sodium selenite (ITS without linoleic acid, Sigma-Aldrich), 50 nM hydrocortisone, 100 U/ml penicillin, and 100 $\mu\text{g}/\text{ml}$ streptomycin (Pen/Strep, Thermo Fisher).

Assessment of renal tubular cell death

LDH release of freshly isolated kidney tubules was measured according to manufacturers' instructions at indicated time points. Briefly, an aliquot of the supernatant was taken, and Lysis Solution was added for 45 min to induce maximal LDH release before another aliquot of the supernatant was taken. Next, the supernatants were incubated with CytoTox 96[®] Reagent for 15 min protected from light at room temperature before adding Stop Solution. Absorbance was measured at 490 nm.

All performed experiments concerning isolated murine renal tubules contain a negative control to assess LDH release at 0 h of incubation as quality control. Experiments were considered valid when the negative controls had less than 10% LDH release. Isolated murine renal tubules were placed in 24-well plates containing the respective agents diluted in Dulbecco's Modified Eagle Medium F-12 Nutrient Mixture without glycine and phenol red (DMEM/F-12, custom made by Cell Culture Technologies LLC, Switzerland), supplemented with 0.01 mg/ml recombinant human insulin, 5.5 $\mu\text{g}/\text{ml}$ human transferrin, 0.005 $\mu\text{g}/\text{ml}$ sodium selenite (ITS without linoleic acid, Sigma-Aldrich), 50 nM hydrocortisone, 100 U/ml penicillin, and 100 $\mu\text{g}/\text{ml}$ streptomycin (Pen/Strep, Thermo Fisher). After indicated time points, the medium of each well was collected, and tubules were prepared for LDH release assay. Images of the treated murine renal tubules were obtained using a $\times 20/0.30$ PH1 objective on a Leica DMI1 microscope.

Statistics

Statistical analyses were performed using Prism 8 (GraphPad software, San Diego, CA, USA). To test the null hypothesis of no difference between groups in the survival experiments, we plotted the animals in a Kaplan–Meier curve and used the log-rank test for statistics. In all other experiments, two-tailed parametric *t*-test was used for normally distributed datasets, and one-way ANOVA followed by post hoc Tukey's multiple comparisons test was used for analyzing data to compare multiple groups. Data were considered significant when $*p \leq 0.05$, $**p \leq 0.01$, or $***p \leq 0.001$. If not otherwise indicated, bar graphs represent the mean plus standard deviation.

Reporting summary

Further information on research design is available in the Nature Research Reporting Summary linked to this article.

DATA AVAILABILITY

The authors confirm that all data required to evaluate the conclusions of this study are presented in the paper and/or the Supplementary Materials. Other data are available from the corresponding author upon reasonable request.

REFERENCES

- Ronco C, Bellomo R, Kellum JA. Acute kidney injury. *Lancet* (Lond, Engl). 2019;394:1949–64.
- Chawla LS, Bellomo R, Bihorac A, Goldstein SL, Siew ED, Bagshaw SM, et al. Acute kidney disease and renal recovery: consensus report of the Acute Disease Quality Initiative (ADQI) 16 Workgroup. *Nat Rev Nephrol*. 2017;13:241–57.
- de Boer IH, Alpers CE, Azeloglu EU, Balis UGJ, Barasch JM, Barisoni L, et al. Rationale and design of the Kidney Precision Medicine Project. *Kidney Int*. 2021;99:498–510.
- Venkatachalam MA, Weinberg JM, Kriz W, Bidani AK. Failed tubule recovery, AKI-CKD transition, and kidney disease progression. *J Am Soc Nephrol*. 2015;26:1765–76.
- Conrad M, Angeli JP, Vandenabeele P, Stockwell BR. Regulated necrosis: disease relevance and therapeutic opportunities. *Nat Rev Drug Discov*. 2016;15:348–66.
- Yuan J, Najafov A, Py BF. Roles of caspases in necrotic cell death. *Cell*. 2016;167:1693–704.
- Kaiser WJ, Upton JW, Long AB, Livingston-Rosanoff D, Daley-Bauer LP, Hakem R, et al. RIP3 mediates the embryonic lethality of caspase-8-deficient mice. *Nature*. 2011;471:368–72.
- Oberst A, Dillon CP, Weinlich R, McCormick LL, Fitzgerald P, Pop C, et al. Catalytic activity of the caspase-8-FLIP(L) complex inhibits RIPK3-dependent necrosis. *Nature*. 2011;471:363–7.

9. Zhang Z, Zhang Y, Xia S, Kong Q, Li S, Liu X, et al. Gasdermin E suppresses tumour growth by activating anti-tumour immunity. *Nature*. 2020;579:415–20.
10. Demarco B, Grayczyk JP, Bjanec E, Le Roy D, Tonnus W, Assenmacher CA, et al. Caspase-8-dependent gasdermin D cleavage promotes antimicrobial defense but confers susceptibility to TNF-induced lethality. *Sci Adv*. 2020;6:eabc3465.
11. Broz P, Pelegrin P, Shao F. The gasdermins, a protein family executing cell death and inflammation. *Nat Rev Immunol*. 2020;20:143–57.
12. Yang J, Liu Z, Wang C, Yang R, Rathkey JK, Pinkard OW, et al. Mechanism of gasdermin D recognition by inflammatory caspases and their inhibition by a gasdermin D-derived peptide inhibitor. *Proc Natl Acad Sci USA*. 2018;115:6792–7.
13. Schneider KS, Gross CJ, Dreier RF, Saller BS, Mishra R, Gorka O, et al. The inflammasome drives GSDMD-independent secondary pyroptosis and IL-1 release in the absence of caspase-1 protease activity. *Cell Rep*. 2017;21:3846–59.
14. Kayagaki N, Stowe IB, Lee BL, O'Rourke K, Anderson K, Warming S, et al. Caspase-11 cleaves gasdermin D for non-canonical inflammasome signalling. *Nature*. 2015;526:666–71.
15. Degterev A, Hitomi J, Germscheid M, Ch'en IL, Korkina O, Teng X, et al. Identification of RIP1 kinase as a specific cellular target of necrostatins. *Nat Chem Biol*. 2008;4:313–21.
16. Zhang H, Zhou X, McQuade T, Li J, Chan FK, Zhang J. Functional complementation between FADD and RIP1 in embryos and lymphocytes. *Nature*. 2011;471:373–6.
17. Cho YS, Challa S, Moquin D, Genga R, Ray TD, Guildford M, et al. Phosphorylation-driven assembly of the RIP1-RIP3 complex regulates programmed necrosis and virus-induced inflammation. *Cell*. 2009;137:1112–23.
18. He S, Wang L, Miao L, Wang T, Du F, Zhao L, et al. Receptor interacting protein kinase-3 determines cellular necrotic response to TNF- α . *Cell*. 2009;137:1100–11.
19. Zhang DW, Shao J, Lin J, Zhang N, Lu BJ, Lin SC, et al. RIP3, an energy metabolism regulator that switches TNF-induced cell death from apoptosis to necrosis. *Science*. 2009;325:332–6.
20. Sun L, Wang H, Wang Z, He S, Chen S, Liao D, et al. Mixed lineage kinase domain-like protein mediates necrosis signaling downstream of RIP3 kinase. *Cell*. 2012;148:213–27.
21. Zhao J, Jitkaew S, Cai Z, Choksi S, Li Q, Luo J, et al. Mixed lineage kinase domain-like is a key receptor interacting protein 3 downstream component of TNF-induced necrosis. *Proc Natl Acad Sci USA*. 2012;109:5322–7.
22. Gong Y-N, Guy C, Olauson H, Becker JU, Yang M, Fitzgerald P, et al. ESCRT-III acts downstream of MLKL to regulate necroptotic cell death and its consequences. *Cell*. 2017;169:286–300.e16.
23. Yoon S, Kovalenko A, Bogdanov K, Wallach D. MLKL, the protein that mediates necroptosis, also regulates endosomal trafficking and extracellular vesicle generation. *Immunity*. 2017;47:51–65.e7.
24. Shi J, Zhao Y, Wang K, Shi X, Wang Y, Huang H, et al. Cleavage of GSDMD by inflammatory caspases determines pyroptotic cell death. *Nature*. 2015;526:660–5.
25. Ding J, Wang K, Liu W, She Y, Sun Q, Shi J, et al. Pore-forming activity and structural autoinhibition of the gasdermin family. *Nature*. 2016;535:111–6.
26. Aglietti RA, Estevez A, Gupta A, Ramirez MG, Liu PS, Kayagaki N, et al. GsdmD p30 elicited by caspase-11 during pyroptosis forms pores in membranes. *Proc Natl Acad Sci USA*. 2016;113:7858.
27. Evavold CL, Ruan J, Tan Y, Xia S, Wu H, Kagan JC. The pore-forming protein Gasdermin D regulates interleukin-1 secretion from living macrophages. *Immunity*. 2018;48:35–44.e6.
28. Heilig R, Dick MS, Sborgi L, Meunier E, Hiller S, Broz P. The Gasdermin-D pore acts as a conduit for IL-1 β secretion in mice. *Eur J Immunol*. 2018;48:584–92.
29. Zheng M, Karki R, Vogel P, Kanneganti T-D. Caspase-6 is a key regulator of innate immunity, inflammasome activation, and host defense. *Cell*. 2020;181:674–87.e13.
30. Kaiser WJ, Upton JW, Mocarski ES. Viral modulation of programmed necrosis. *Curr Opin Virol*. 2013;3:296–306.
31. Newton K, Wickliffe KE, Maltzman A, Dugger DL, Reja R, Zhang Y, et al. Activity of caspase-8 determines plasticity between cell death pathways. *Nature*. 2019;575:679–682.
32. Zheng J, Conrad M. The metabolic underpinnings of ferroptosis. *Cell Metab*. 2020;32:920–937.
33. Stockwell BR, Friedmann Angeli JP, Bayir H, Bush AI, Conrad M, Dixon SJ, et al. Ferroptosis: a regulated cell death nexus linking metabolism, redox biology, and disease. *Cell*. 2017;171:273–85.
34. Katikaneni A, Jelcic M, Gerlach GF, Ma Y, Overholtzer M, Niethammer P. Lipid peroxidation regulates long-range wound detection through 5-lipoxygenase in zebrafish. *Nat Cell Biol*. 2020;22:1049–55.
35. Kim SE, Zhang L, Ma K, Riegman M, Chen F, Ingold I, et al. Ultrasmall nanoparticles induce ferroptosis in nutrient-deprived cancer cells and suppress tumour growth. *Nat Nanotechnol*. 2016;11:977–985.
36. Riegman M, Bradbury MS, Overholtzer M. Population dynamics in cell death: mechanisms of propagation. *Trends Cancer*. 2019;5:558–68.
37. Riegman M, Sagie L, Galed C, Levin T, Steinberg N, Dixon SJ, et al. Ferroptosis occurs through an osmotic mechanism and propagates independently of cell rupture. *Nat Cell Biol*. 2020;22:1042–1048.
38. Linkermann A, Skouta R, Himmerkus N, Mulay SR, Dewitz C, De Zen F, et al. Synchronized renal tubular cell death involves ferroptosis. *Proc Natl Acad Sci USA*. 2014;111:16836–41.
39. Belavgeni A, Meyer C, Stumpf J, Hugo C, Linkermann A. Ferroptosis and necroptosis in the kidney. *Cell Chem Biol*. 2020;27:448–62.
40. Mulay SR, Linkermann A, Anders HJ. Necroinflammation in kidney disease. *J Am Soc Nephrol*. 2016;27:27–39.
41. Linkermann A, Chen G, Dong G, Kundendorf U, Krautwald S, Dong Z. Regulated cell death in AKI. *J Am Soc Nephrol*. 2014;25:2689–701.
42. Li Y, Xia W, Wu M, Yin J, Wang Q, Li S, et al. Activation of GSDMD contributes to acute kidney injury induced by cisplatin. *Am J Physiol Ren Physiol*. 2020;318:F96–f106.
43. Miao N, Yin F, Xie H, Wang Y, Xu Y, Shen Y, et al. The cleavage of gasdermin D by caspase-11 promotes tubular epithelial cell pyroptosis and urinary IL-18 excretion in acute kidney injury. *Kidney Int*. 2019;96:1105–20.
44. Tonnus W, Linkermann A. Gasdermin D and pyroptosis in acute kidney injury. *Kidney Int*. 2019;96:1061–3.
45. Xia W, Li Y, Wu M, Jin Q, Wang Q, Li S, et al. Gasdermin E deficiency attenuates acute kidney injury by inhibiting pyroptosis and inflammation. *Cell Death Dis*. 2021;12:139.
46. Zhang Z, Shao X, Jiang N, Mou S, Gu L, Li S, et al. Caspase-11-mediated tubular epithelial pyroptosis underlies contrast-induced acute kidney injury. *Cell Death Dis*. 2018;9:983.
47. Conos SA, Chen KW, De Nardo D, Hara H, Whitehead L, Nunez G, et al. Active MLKL triggers the NLRP3 inflammasome in a cell-intrinsic manner. *Proc Natl Acad Sci USA*. 2017;114:E961–E969.
48. Fritsch M, Günther SD, Schwarzer R, Albert M-C, Schorn F, Werthenbach JP, et al. Caspase-8 is the molecular switch for apoptosis, necroptosis and pyroptosis. *Nature*. 2019;575:683–687.
49. Doerflinger M, Deng Y, Whitney P, Salvamoser R, Engel S, Kueh AJ, et al. Flexible usage and interconnectivity of diverse cell death pathways protect against intracellular infection. *Immunity*. 2020;53:533–547.e7.
50. Linkermann A, Brasen JH, Himmerkus N, Liu S, Huber TB, Kundendorf U, et al. Rip1 (receptor-interacting protein kinase 1) mediates necroptosis and contributes to renal ischemia/reperfusion injury. *Kidney Int*. 2012;81:751–61.
51. Linkermann A, Brasen JH, Darding M, Jin MK, Sanz AB, Heller JO, et al. Two independent pathways of regulated necrosis mediate ischemia-reperfusion injury. *Proc Natl Acad Sci USA*. 2013;110:12024–9.
52. von Mässenhausen A, Tonnus W, Himmerkus N, Parmentier S, Saleh D, Rodriguez D, et al. Phenytoin inhibits necroptosis. *Cell Death Dis*. 2018;9:359.
53. Summers SA, Chan J, Gan PY, Dewage L, Nozaki Y, Steinmetz OM, et al. Mast cells mediate acute kidney injury through the production of TNF. *J Am Soc Nephrol*. 2011;22:2226–36.
54. Zhang B, Ramesh G, Norbury CC, Reeves WB. Cisplatin-induced nephrotoxicity is mediated by tumor necrosis factor- α produced by renal parenchymal cells. *Kidney Int*. 2007;72:37–44.
55. Ramesh G, Reeves WB. TNF- α mediates chemokine and cytokine expression and renal injury in cisplatin nephrotoxicity. *J Clin Invest*. 2002;110:835–42.
56. Kang TB, Yang SH, Toth B, Kovalenko A, Wallach D. Caspase-8 blocks kinase RIPK3-mediated activation of the NLRP3 inflammasome. *Immunity*. 2013;38:27–40.
57. Kang TB, Yang SH, Toth B, Kovalenko A, Wallach D. Activation of the NLRP3 inflammasome by proteins that signal for necroptosis. *Methods Enzymol*. 2014;545:67–81.
58. Wallach D, Kang TB, Dillon CP, Green DR. Programmed necrosis in inflammation: toward identification of the effector molecules. *Science*. 2016;352:aaf2154.
59. Mandal P, Feng Y, Lyons JD, Berger SB, Otani S, DeLaney A, et al. Caspase-8 collaborates with caspase-11 to drive tissue damage and execution of endotoxin shock. *Immunity*. 2018;49:42–55.e6.
60. Muendlein HI, Jettton D, Connolly WM, Eidell KP, Magri Z, Smirnova I, et al. cFLIPL protects macrophages from LPS-induced pyroptosis via inhibition of complex II formation. *Science*. 2020;367:1379.
61. Orning P, Weng D, Starheim K, Ratner D, Best Z, Lee B, et al. Pathogen blockade of TAK1 triggers caspase-8-dependent cleavage of gasdermin D and cell death. *Science (New York, NY)*. 2018;362:1064–1069.
62. Sarhan J, Liu BC, Muendlein HI, Li P, Nilson R, Tang AY, et al. Caspase-8 induces cleavage of gasdermin D to elicit pyroptosis during Yersinia infection. *Proc Natl Acad Sci USA*. 2018;115:E10888–E10897.
63. Lei X, Zhang Z, Xiao X, Qi J, He B, Wang J. Enterovirus 71 inhibits pyroptosis through cleavage of GSDMD. *J Virol*. 2017;91:e01069–17.
64. Zhang T, Yin C, Boyd DF, Quarato G, Ingram JP, Shubina M, et al. Influenza virus Z-RNAs induce ZBP1-mediated necroptosis. *Cell*. 2020;180:1115–29.e13.

65. Weindel CG, Martinez EL, Zhao X, Mabry CJ, Bell SL, Vail KJ, et al. Mitochondrial ROS promotes susceptibility to infection via gasdermin D-mediated necroptosis. *Cell*. 2022;185:3214–3231.e23.
66. Tonnus W, Meyer C, Steinebach C, Belavgeni A, von Mässenhausen A, Gonzalez NZ, et al. Dysfunction of the key ferroptosis-surveillance systems hypersensitizes mice to tubular necrosis during acute kidney injury. *Nat Commun*. 2021;12:4402.
67. Hu JJ, Liu X, Xia S, Zhang Z, Zhang Y, Zhao J, et al. FDA-approved disulfiram inhibits pyroptosis by blocking gasdermin D pore formation. *Nat Immunol*. 2020;21:736–745.
68. Ningaraj NS, Rao MK. Disulfiram augments oxidative stress in rat brain following bilateral carotid artery occlusion. *J Biomed Sci*. 1998;5:226–30.
69. Abdelkarim GE, Gertz K, Harms C, Katchanov J, Dirnagl U, Szabo C, et al. Protective effects of PJ34, a novel, potent inhibitor of poly(ADP-ribose) polymerase (PARP) in in vitro and in vivo models of stroke. *Int J Mol Med*. 2001;7:255–60.
70. Xiao C, Zhao H, Zhu H, Zhang Y, Su Q, Zhao F, et al. Tisp40 induces tubular epithelial cell GSDMD-mediated pyroptosis in renal ischemia-reperfusion injury via NF- κ B signaling. *Front Physiol*. 2020;11:906.
71. Wang Y, Gao W, Shi X, Ding J, Liu W, He H, et al. Chemotherapy drugs induce pyroptosis through caspase-3 cleavage of a Gasdermin. *Nature*. 2017;547:99–103.
72. Murphy JM, Czabotar PE, Hildebrand JM, Lucet IS, Zhang JG, Alvarez-Diaz S, et al. The pseudokinase MLKL mediates necroptosis via a molecular switch mechanism. *Immunity*. 2013;39:443–53.
73. Tonnus W, Al-Mekhlafi M, Hugo C, Linkermann A. Assessment of in vivo kidney cell death: acute kidney injury. *Methods Mol Biol*. 2018;1857:135–44.
74. Mulay SR, Eberhard JN, Pfann V, Marschner JA, Darisipudi MN, Daniel C, et al. Oxalate-induced chronic kidney disease with its uremic and cardiovascular complications in C57BL/6 mice. *Am J Physiol Ren Physiol*. 2016;310:F785–f95.
75. Schreiber A, Shulhevich Y, Geraci S, Hesser J, Stsepankou D, Neudecker S, et al. Transcutaneous measurement of renal function in conscious mice. *Am J Physiol Ren Physiol*. 2012;303:F783–8.
76. Steiger S, Grill JF, Ma Q, Bäuerle T, Jordan J, Smolle M, et al. Anti-transforming growth factor β IgG elicits a dual effect on calcium oxalate crystallization and progressive nephrocalcinosis-related chronic kidney disease. *Front Immunol*. 2018;9:619.

ACKNOWLEDGEMENTS

We would like to cordially thank Romy Opitz, Anne Pioch, and Céline Laqua for expert technical assistance. We thank the Light Microscopy Facility at Dresden BIOTEC, in particular Hella Hartmann, and the histology facility at the CMCB of the TU Dresden with special acknowledgement of Susanne Weiche and Dana Thatmeyer for expert help.

AUTHOR CONTRIBUTIONS

WT, FM, AB, ML, YK, AB, AvM, CM, SL, FG, KB, and JUB performed experiments and analyzed the data. WT, FM, AB, AvM, PH, CH, H-JA, SRB, FS, and AL designed the

experiments and analyzed the data. FS provided the GSDMD- and GSDME-deficient mice. WT and AL wrote the paper.

FUNDING INFORMATION

Work in the Linkermann Lab is funded by the German Research Foundation (DFG), SFB-TRR 205, SFB-TRR 127, SPP 2306, IRTG 2251, and a Heisenberg-Professorship to AL (project number 324141047). HJA was supported by the Deutsche Forschungsgemeinschaft (AN372/16-2, 27-1, and 30-1). Open Access funding enabled and organized by Projekt DEAL.

COMPETING INTERESTS

The authors declare no competing interests.

ADDITIONAL INFORMATION

Supplementary information The online version contains supplementary material available at <https://doi.org/10.1038/s41419-022-05230-9>.

Correspondence and requests for materials should be addressed to Andreas Linkermann.

Reprints and permission information is available at <http://www.nature.com/reprints>

Publisher's note Springer Nature remains neutral with regard to jurisdictional claims in published maps and institutional affiliations.



Open Access This article is licensed under a Creative Commons Attribution 4.0 International License, which permits use, sharing, adaptation, distribution and reproduction in any medium or format, as long as you give appropriate credit to the original author(s) and the source, provide a link to the Creative Commons license, and indicate if changes were made. The images or other third party material in this article are included in the article's Creative Commons license, unless indicated otherwise in a credit line to the material. If material is not included in the article's Creative Commons license and your intended use is not permitted by statutory regulation or exceeds the permitted use, you will need to obtain permission directly from the copyright holder. To view a copy of this license, visit <http://creativecommons.org/licenses/by/4.0/>.

© The Author(s) 2022